ORIGINALS

K. Parker · K. D. von Ellenrieder · J. Soria

Using stereo multigrid DPIV (SMDPIV) measurements to investigate the vortical skeleton behind a finite-span flapping wing

Abstract The structure of the flow behind wings with finite span (3D) is significantly more complex than the flow behind infinite span (2D) wings. It has been shown that the presence of wingtip vortices behind finite span wings significantly modifies the geometry of the wake flow. It is felt that this modification alters the dynamics of interaction between leading and trailing edge vorticity in a manner that affects the ability of 2D flapping wings to produce thrust. A model of the mean flow skeleton has been proposed from qualitative flow visualization experiments. An unambiguous quantitative representation of the actual flow is required for comparison to the proposed model. To accomplish this the full 3D 3C velocity is required in the volume behind the 3D flapping wing. It is proposed to use stereoscopic multigrid digital particle image velocimetry (SMDPIV) measurements to investigate this unsteady oscillatory flow. This paper reports preliminary SMDPIV measurements along the plane of a symmetrical NACA-profile wing at a Strouhal number of 0.35. Phase averaged measurements are used to investigate the complex flow topology and the influence of the forcing flow on the evolution of the large scale structure of a jet-flow. This paper focuses on optimizing the SMDPIV experimental methodology applied to liquid flows. By refining the 2D 3C technique, the 3D topology of the flow can be investigated with a high degree of accuracy and repeatability. Preliminary results show that the flow is characterized by two pairs of coherent structures of positive and negative vorticity. The arrangement of these structures in the flow is controlled by the motion of the wing. Vorticity of opposite

rotation is shed at the extreme heave and pitch positions of the aerofoil to set up a thrust indicative vortex street in support of the suggested topological model.

1 Introduction

Nature has, through many thousands of years of testing and redesign, optimized many of the aero-fluid engineering problems encountered by researchers today. For this reason aspects of insect and fish locomotion have been extensively studied. An understanding of cetacean locomotion has raised the argument whether it could be mimicked in alternate propulsion. More specifically, the study of fluid dynamical aspects of carangiform motion, characterized by the undulating motion of the tail fin propulsion, has raised the question whether any principles from these studies can be applied to engineering applications (Drucker and Lauder 2001; Triantafyllou et al. 1993). The concept of biomimetic engineering does not preclude any complex fluid mechanical refinements which necessitates a greater understanding of the physics responsible for the assumed optimal efficiency of propulsion in nature (Jones et al. 1998).

Flapping is described as simultaneous heave and pitch oscillations of a tail fin or wing. The study of flapping wings allows further insight into other aero-fluid dynamic problems, specifically in the unsteady flow regime. For example, aeroelastic flutter is still a major problem in modern aircraft and is caused by the coupled interaction of the structural dynamics and the aerodynamics of the vehicle (Katz and Weihz 1978). Unsteady loading of turbo-machinery components remains a major problem in the area of power generation. All these areas are related to vorticity generation, whether undesirable or purposeful. The study of pure heaving, pure pitching or combinations of heaving and pitching aerofoils is a starting point for understanding and overcoming these problems. Furthermore, the potential for

K. Parker (✉) · J. Soria
Laboratory for Turbulence Research in Aerospace & Combustion,
Mechanical Engineering, Monash University,
Clayton Campus, Melbourne, VIC, 3800, Australia
E-mail: Kamal.Parker@eng.Monash.edu.au

K. D. Ellenrieder
Department of Ocean Engineering,
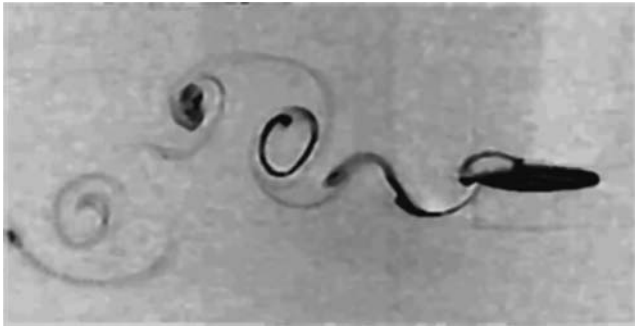Florida Atlantic University, Dania Beach,
FL 33004-3023, USA

Fig. 1 Dye flow visualization of the flow behind a 2D flapping aerofoil at $St = 0.35$

Fig. 3 Proposed vortex skeleton behind a finite aspect ratio flapping aerofoil (von Ellenrieder et al. 2003)

modification of the large scale structures in propulsive wakes presents a useful method of control of vortex generation in jet flows through dynamic redistribution. Control can be accomplished through forced oscillation of an aerofoil affecting its own jet or in a tandem arrangement with another lifting surface (Gopalkrishnan et al. 1994; Jones et al. 1998). In these cases the development of the boundary layer and the separated flow can be modified by regulating the oscillations of the forced body. Here the focus is on dynamic flow control through vorticity redistribution.

2D flapping wings have been extensively studied. Noteworthy experimental (Anderson et al. 1998; DeLaurier and Harris 1982; Karpouzian et al. 1990) and numerical (Jones et al. 2002, 1998; Ramamurti and Sandberg 2001) studies have explored the influence of various aspects of the forced oscillation on the ability of a flapping wing to produce thrust, as well as correlating lunate locomotion with propulsion. These studies have managed to quantify the level of thrust that can be achieved with flapping aerofoils. Up to 80% thrust efficiency has been recorded (Anderson et al. 1998). The
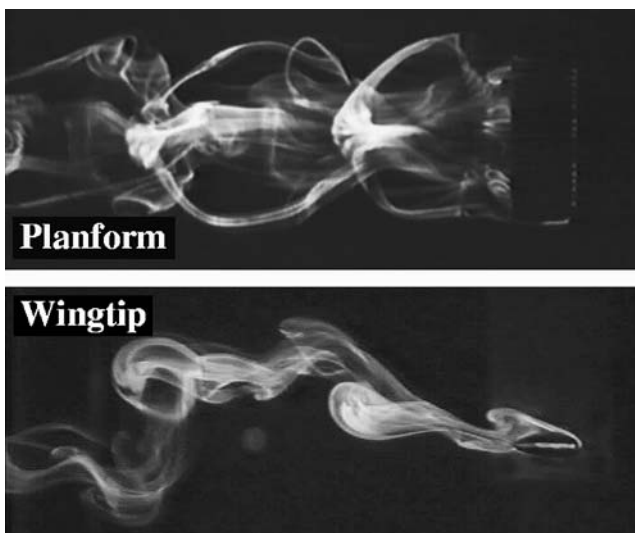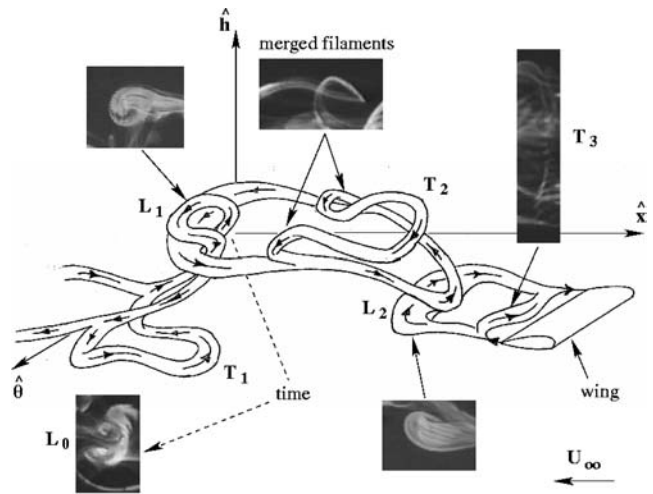
influence of vorticity redistribution on propulsive efficiency has been discussed in the context of the observed 2D jet-flows. While some previous numerical experiments have studied the effect of wing three dimensionality and flexibility, the focus has been primarily on development of some adaptive thin aerofoil theory for prediction of thrust on finite span flapping wings (Platzer 2001). A collaborative effort between Jones et al. (2002) providing the experimental results and Neef et al.
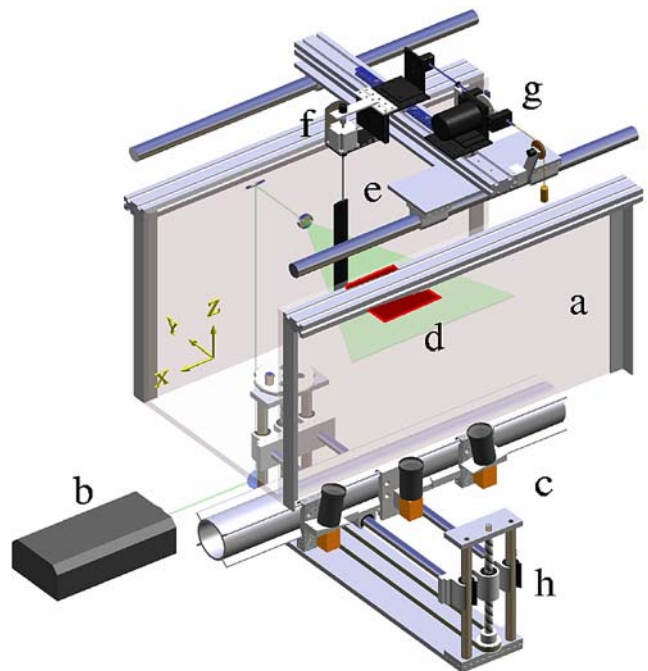

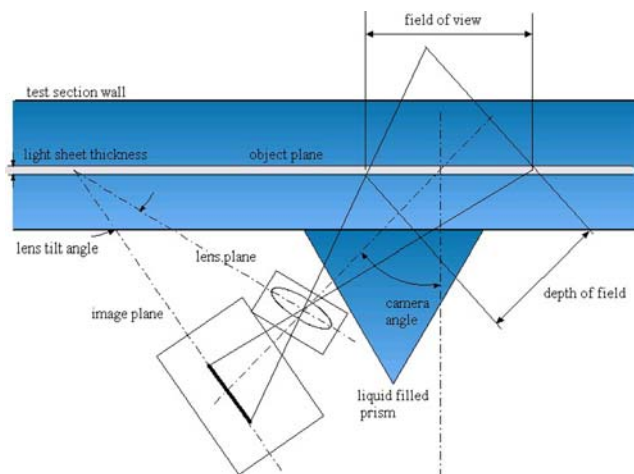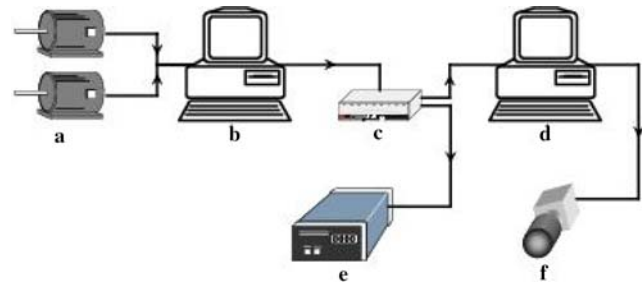**Fig. 4** Schematic of the experimental apparatus. **a** Test section. **b** Laser. **c** Stereo-CCD camera arrangement. **d** Horizontal light sheet with central measurement region highlighted. **e** Wing mounted on vertical translation stage. **f** Pitch stepper motor. **g** Heave stepper motor with scotch-yoke. **h** Three-axis translation stage

Fig. 2 Dye flow visualization of the flow behind a 3D flapping foil

Table 1 Experimental setup parameters

Parameter	Quantity
c	20 mm
AR	3
St	0.35
Re_c	700
θ_0	5°
h_0	$c/2$ mm
θ_{pitch}	0.005°
θ_{heave}	0.0063°
z_s	0.0254 mm

Fig. 6 Schematic of the image acquisition system for the stereo experiments. **a** Trigger signal from stepper motors. **b** RT Linux control PC. **c** Breakout box. **d** Camera control PC. **e** Nd:Yag laser. **f** CCD cameras

providing results from several numerical approaches explored some aspects of three-dimensionality. The focus of this study was to evaluate the ability of various numerical schemes to identify important aspects of the flow physics from experimental data. The experiments were conducted at $Re > 50{,}000$ corresponding to the flight of certain species of birds. The study found that the wing aspect ratio and Strouhal number control the thrust produced. The study did not comment on the flow physics at lower Reynolds numbers which are very costly in terms of computational effort as well as the limited ability of the Euler/Navier-Stokes solvers. In general, significantly fewer attempts have been made to correlate the ability of 3D wings to produce thrust with the vortex evolutionary process.

Ohmi et al. (1991, 1990) studied the vortex formation around heaving and pitching aerofoils at Reynolds numbers less than 10,000 and found that the vortex wake patterns depended on a product of the dimensionless oscillation frequency and the oscillation amplitude. This parameter is closely related to the dimensionless Strouhal number (also referred to in a modified form as reduced frequency) which is also influential in the thrust producibility of flapping wings. In a Strouhal regime of $0.25 \leq St \leq 0.35$ 2D aerofoils produce thrust with maximum efficiency (Anderson et al.

1998). Ohmi et al. (1990) found the Reynolds number to be of secondary importance in the formation of the wake patterns. An increase in Reynolds number would increase the range of scales in the flow due to an increase in the smaller scales but not alter the large scale structure of the flow. Extensive studies on unsteady aerofoils by McCroskey (1982) also tend to agree with others (Anderson et al. 1998) that effect of Reynolds number is very small compared to the Strouhal number St defined as,

$$St = \frac{fA}{U_\infty}, \tag{1}$$

where f equals the frequency of oscillation (heave frequency equals pitch frequency), A represents the maximum excursion of the aerofoil trailing edge (which is the double-amplitude of oscillation equal to c) and U_∞ represents the free-stream velocity. From 2D aerofoil experiments the flow behind a thrust producing wing is described by a 'reverse' Karman vortex street, where the mean velocity profile resembles a jet when momentum is added to the flow (Koochesfahani 1989). In reality, wings are three dimensional and have finite spans. In this case the wingtip vortices are expected to reduce any estimate of thrust efficiency based on 2D wing measurements (Cheng and Murillo 1984). It is further expected that the hydrodynamics are altered through the interaction of wingtip vortices with any 2D vortices.

Figure 1 shows a typical qualitative flow visualization observed from the wingtip of an infinite-span aerofoil. The roll-up of the dye filaments emanating from regions of the aerofoil's leading and trailing edges is clearly

Fig. 5 Schematic indicating the Scheimpflug condition and the effect of the liquid filled prism on the stereo imaging

Table 2 PIV image acquisition and analysis parameters

Parameter	Quantity
dt	7.0 ms
Grid spacing	16 px
IW_0	32 px
IW_1	24 px
MVR	0.25
MVC	1.3
dof	8.0 px

Table 3 RMS [*px*] error from solid body translations of 1 mm

RMS	$\sigma\Delta x$	$\sigma\Delta y$	$\sigma\Delta z$
1 mm X	0.056	0.005	0.101
1 mm Y	0.01	0.064	0.088
1 mm Z	0.053	0.023	0.193

visible. In contrast, the presence of wingtip vortices significantly alter the typical 2D vortex sheet as shown in Fig. 2. The experimental parameters are similar in both cases, where the flow is from right to left. In Fig. 2 the flow is observed from planform and wingtip perspectives. In both cases the $St = 0.35$ and the images are taken at the same heave and pitch orientation of a NACA0030 aerofoil. The structure of the flow is significantly more complex with considerably more spanwise activity for the 3D case than for the 2D case.

A parametric dye-flow visualization study by the present authors (Parker et al. 2002, 2003a, 2003b) has culminated in a geometric model of the vortical skeleton for a 3D thrust-producing flapping wing (von Ellenrieder et al. 2003). It is found that pairs of leading (L) and trailing edge (T) vortices interact with wing tip vortices to create a distinct skeletal structure over one oscillation cycle, which is shown in Fig. 3. The subscripts 1, 2 and 3 represent the respective pair of vortical structures to which L or T belong. The direction of circulation is inferred from the motion of the aerofoil and the direction of the dye roll-up. Since dye is a passive scalar and flow visualizations in an unsteady flow are ambiguous in the information that they provide, more quantitative experiments are necessary to confirm the proposed vortical model. Nonetheless, several recent numerical studies have predicted very similar flow patterns (Blondeaux et al. 2005; Dong et al. 2005) but have recommended further quantitative measurements.

The results presented in this paper are part of a larger study to unambiguously identify the structures in a complex 3D 'jet' of a thrust producing wing. The

Fig. 8 Error $\varepsilon_{\Delta y}$ between the true x_2 displacement in the object plane and the computed value

interaction of these structures are described in the context of the proposed model in Fig. 3. The aim of the study is to explore the influence of forced oscillation on the flow structures in a phase-averaged sense.

To quantitatively analyse this highly vortical jet flow, stereoscopic multigrid digital particle image velocimetry (SMDPIV) is used since it provides all three components of velocity in a single 2D plane. This paper reports on the application of the SMDPIV technique to flapping foils in liquid flows. The experimental methodology is discussed in detail with specific focus on the application of SMDPIV in the local experimental water tunnel facility and the difficulties associated with measurement over large volumes of water. The SMDPIV validation methodology is described and the uncertainties in the resolved three components of velocity are presented. Thereafter, some results from the SMDPIV experiments applied to the flow behind a 3D thrust-producing flapping wing along the plane of symmetry are presented and discussed.
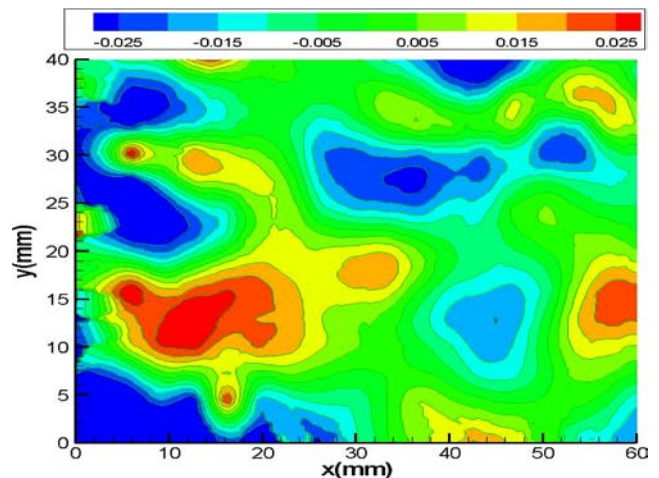

Fig. 7 Error $\varepsilon_{\Delta x}$ between the true x_1 displacement in the object plane and the computed value

Fig. 9 Error $\varepsilon_{\Delta z}$ between the true x_3 displacement in the object plane and the computed value

Table 4 RMS [px] mapping and residual error

Error	ΔX^1	ΔY^1	ΔX^2	ΔY^2
Mapping	0.102	0.080	0.209	0.106
Residual	0.0008	0.0064	0.0006	0.0063

Table 5 Phase information where PIV data is acquired

Figure label	Phase	$h(t)$	$\theta(t)$
a	1	$+c$	0
b	2	$+c/2$	$+\theta_0/2$
c	3	0	$+\theta_0$
d	4	$-c/2$	$+\theta_0/2$
e	5	$-c$	0
f	6	$-c/2$	$-\theta_0/2$
g	7	0	$-\theta_0$
h	8	$+c/2$	$-\theta_0/2$

2 Experimental technique

2.1 Apparatus and method

The experiments are conducted in the 500 mm recirculating horizontal water tunnel at the Laboratory for Turbulence Research for Aerospace & Combustion. The test section measures 500×500×5,000 mm. The turbulence intensity level in the core region of the test section is less than 0.35% at a mean freestream velocity of 30 mm/s. The properties of the test section are discussed in greater detail in Parker et al. (2004b).

In order to compare the quantitative results presented here to the model proposed by von Ellenrieder et al. (2003), a similar NACA0030-type aerofoil is suspended vertically above the test section as shown in Fig. 4. Table 1 provides pertinent values of the test parameters for this experiment. The aerofoil performs angular (pitch) and lateral (heave) oscillations using stepper motors. The aerofoil heaves in the y direction and simultaneously pitches about its quarter-chord axis. The heave-stepper motor is coupled to a scotch yoke mechanism. The scotch yoke wheel can be adjusted to accommodate different heave oscillation amplitudes. The scotch yoke arm reciprocates a platform which is mounted on precision linear bearings. The motor responsible for aerofoil pitch oscillations is mounted on this platform. The pitch motor drives the aerofoil directly. An in-house
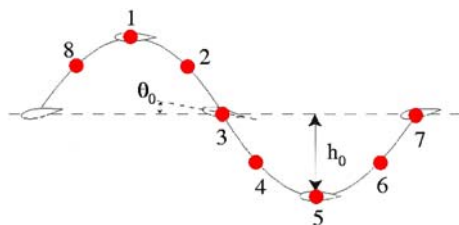

Fig. 10 Motion profile of the flapping wing highlighting the location of the phase averaged measurements
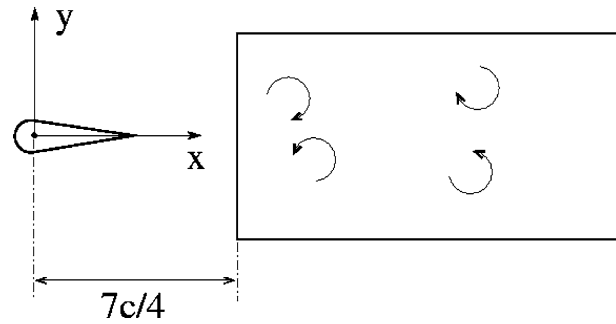
Fig. 11 Cartesian reference frame of measurements

developed motion control program allows different motion parameters (such as frequency f, maximum pitch oscillation amplitude θ_0, and phase angle between heaving and pitching oscillations ψ) to be independently varied. Together with the experimental setup, a selected St or motion profile may be achieved through infinite variations of flow speed and oscillation frequencies. Errors in the pitch and heave oscillations are θ_{pitch} and θ_{heave}, respectively, and are indicative of the level of confidence in the ability of the experimental rig to move the aerofoil to a prescribed location. The entire oscillating mechanism is mounted on a railing system above the water tunnel, allowing the aerofoil setup to be moved to different streamwise locations, while the cameras and laser arrangement can be fixed at a particular region of interest in the flow. For this study, the trajectory of the wing study resembles a cosine curve in which,

$$h(t) = h_0 \cos(\omega t), \tag{2}$$

$$\theta(t) = \theta_0 \cos(\omega t + \psi), \tag{3}$$

where $h_0 = c/2$ and $\omega = 2\pi f$ (equal for heave and pitch oscillations). The experimental parameters in Table 1 are selected since it has been shown that 2D aerofoils produce optimal thrust at this condition (Anderson et al. 1998). Furthermore, under these conditions the 'jet' flow structure is significantly altered for a 3D wing as compared to the 2D case (von Ellenrieder et al. 2003).
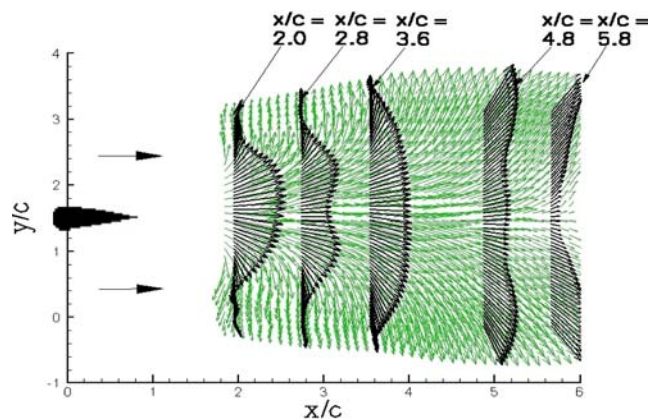
Fig. 12 Mean jet-velocity profile at various downstream stations in the flow field behind a 3D flapping foil
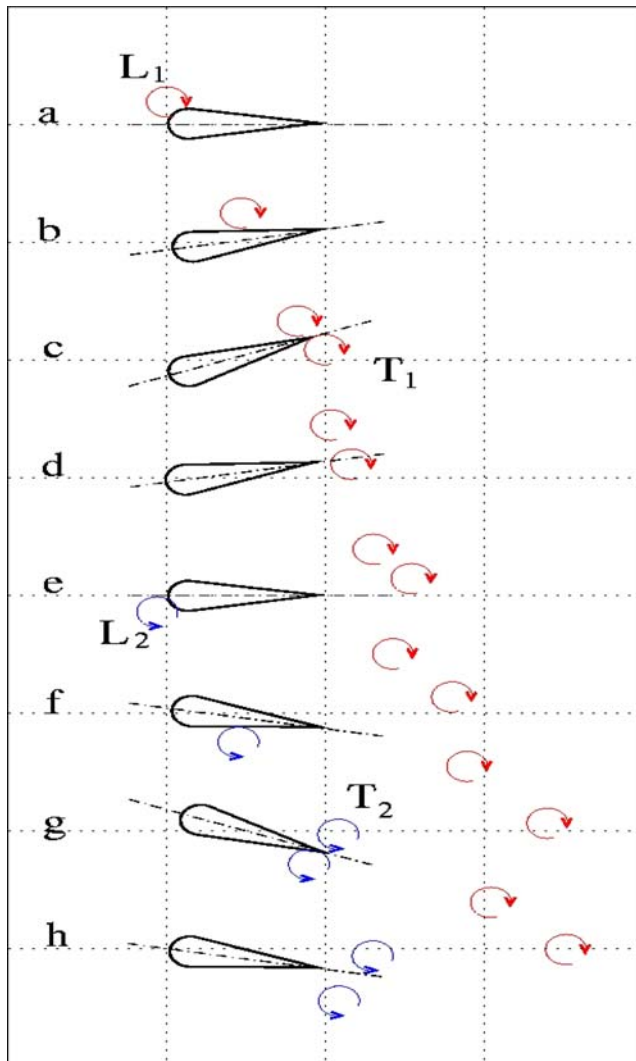
Fig. 13 Evolution of vorticity behind a 3D flapping wing at $St = 0.35$

Potentiometers are mounted in-line with the drive shafts of the heave and pitch stepper motors for the purpose of providing continuous feedback of the output motion of the wings. Furthermore, optical sensors are located at the $h = 0$, $h = h_0$ and $\theta = \theta_0$ locations of the wing trajectory. These sensors provide the trigger signals to initiate the entire PIV image acquisition part. The signal from the sensors further provide a second check of the frequency and phase lag ψ of the wing motion. The present setup facilitates measurements of the flow at various spanwise (z) locations through the use of a vertically mounted linear translation stage. This device permits accurate micro-adjustment up to z_s, mentioned in Table 1. Once focussed and fine tuned, the laser and stereo camera arrangement is fastened firmly into this x,y plane position. Only the wing is allowed to move in the z direction for different spanwise measurements. This arrangement and procedure ensures repeatability of the experiments with minimal interference.

2.2 SMDPIV data acquisition system

Stereoscopic multigrid digital particle image velocimetry measurements are conducted in the near wake region of the foil. A region $4c$ (y direction) by $3c$ (x direction) is captured at a magnification M of 0.1, where $M = $ (object size)/(CCD array size). Previous flow visualizations by Parker et al. (2002) suggest that this measurement area is adequate to capture the large scale structures in the flow over one complete forced oscillation cycle of the foil.

As shown in Fig. 4, three Pixelfly CCD cameras with array sizes of $1{,}280 \times 1{,}024$ px each, are mounted vertically onto a three-axis translation stage below the test section. Note the orientation of the x, y and z axes. An angular-displacement stereo configuration is utilized with the stereo-cameras at 68° to each other. This angular arrangement, according to Lawson and Wu (1997), is suggested for minimizing the total error in the resolved velocity components below 2%. The centre camera is used for standard 2D PIV as well as a 'check' to compare with the SMDPIV velocity vector field results. This helps to 'fine tune' the setup parameters for the SMDPIV experiments. The three CCD cameras are mounted in such a manner to view the same area in the desired plane of measurement. Each camera is fitted with a 55 mm Micro Nikkor Nikon lens. For stereo acquisition the aperture is operated at $f\#8$ for adequate light intensity. To satisfy the Scheimpflug condition and get uniform focus in the distorted stereo images, each camera axis is tilted by 3°. At this condition Fig. 5 shows that the image plane, object plane and lens plane intersect at a point in the object plane.

Potters hollow glass beads nominally 11 μm in diameter are used to seed the water tunnel. The particles are illuminated by a laser light from a dual-cavity Nd:Yag laser (New Wave, CA, USA), pulsing 532 nm light at 32 mJ. With the necessary optics, a 3 mm thick horizontal light sheet is created in the midspan region of the aerofoil (see Fig. 4). A beam collector is placed on the far side wall of the test section to collect stray light from the laser. Due to the problem of index of refraction mismatch of air–liquid–glass when viewing liquid flows, the stereo images are radially distorted and particles appear as ellipses (Prasad 2000). To overcome this problem and achieve uniform magnification across the imaged field, the test section floor is modified by mounting a liquid filled prism to the bottom, as shown in Fig. 5. The flow is viewed through the prism face which is inclined at the camera angle. Any air gaps between the perspex surfaces of the test section floor and the prism wall are filled with a mixture of water and glycerine. The index of refraction of the mixture is matched to that of the perspex, typically 0.51.

2.3 PIV data analysis

The first part of SMDPIV involves simultaneous acquisition of images from each stereo camera, as in the

Fig. 14 (*top*) Instantaneous dye flow visualization at $St = 0.35$ for phase 1. (*centre*) Integrated streamline pattern for the $\langle u \rangle$, $\langle v \rangle$ in-plane velocity components, superimposed with out-of-plane vorticity contours. (*bottom*) u, v velocity vector field shaded by the $\langle w \rangle$ velocity component behind a 3D flapping wing at phase 1 location along the oscillation trajectory. In all cases the velocity components are non-dimensionalised by the freestream velocity U_∞
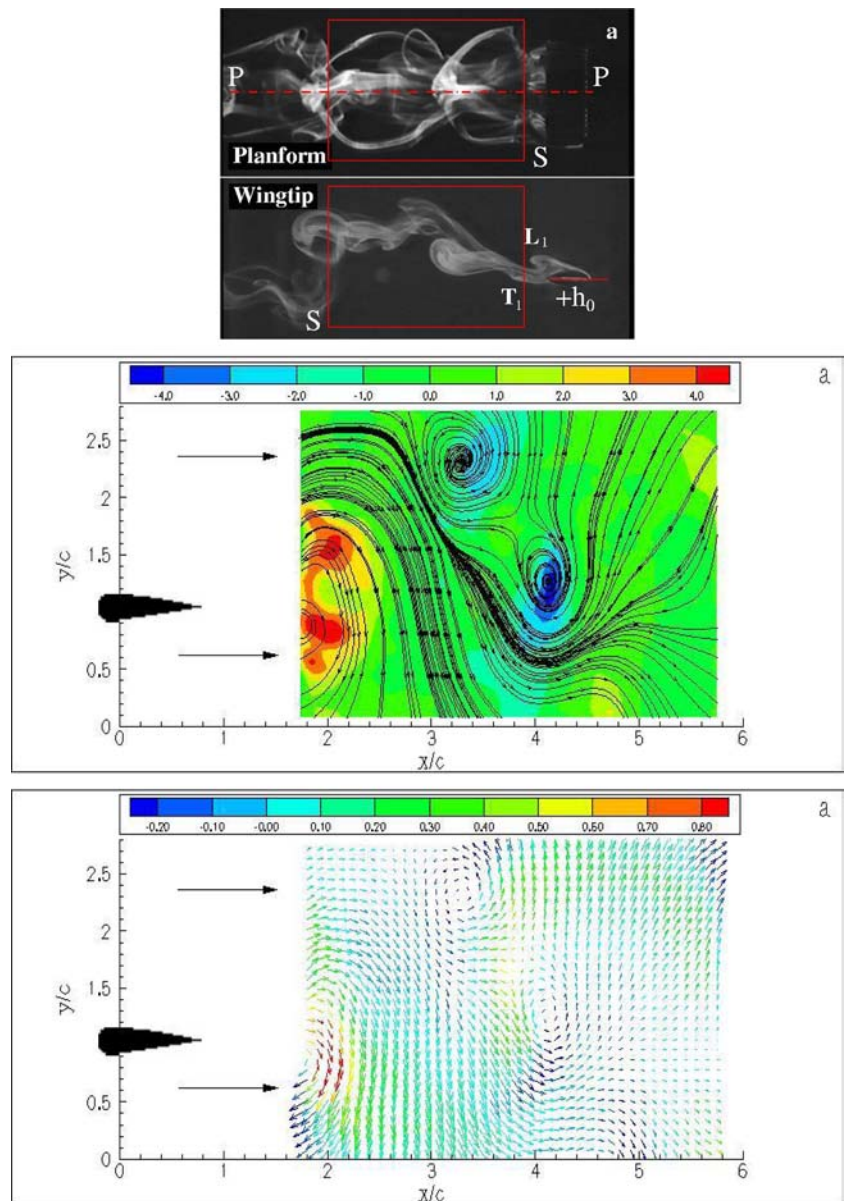

case of standard 2D PIV. The images are analysed using a multi-grid cross correlation digital particle image velocimetry algorithm (MCCDPIV) described by Soria (1996). Using an adaptive and iterative correlation scheme applied to a hierarchy of regular shaped interrogation windows over the double exposed PIV images, the displacement of particles are determined with a high degree of accuracy. The details, performance and uncertainty of the MCCDPIV algorithm with applications to the analysis of single and double exposed PIV images as well as holographic PIV images are reported in Soria (1996), Soria et al. (2003), and von Ellenrieder et al. (2001).

For the results presented here, single exposed image pairs are acquired in single planes along the span of the aerofoil (*z*-direction). The laser firing is synchronized with the motion of the aerofoil. Figure 6 shows the basic

acquisition sequence. The motion of the stepper motors activate the optical sensors mounted at specific locations along the trajectory. A 5-V trigger signal is relayed through the parallel port of a RT Linux control computer via a breakout box. The RT Linux controller manages the entire laser firing and image acquisition process. The camera shutters are instructed to open and the laser fires two pulses separated by a specified time. The camera shutter closes and the two acquired images are downloaded to the hard drive. The process is repeated once another trigger signal is received from the sensors. The current arrangement is relatively cost effective with the added flexibility providing experimental repeatability.

Images are acquired at eight equally spaced locations within one heave cycle. The period of one heave cycle is 2,000 ms. Table 2 indicates the interrogation parameters

Fig. 15 (*top*) Instantaneous dye flow visualization at $St = 0.35$ for phase 2. (*centre*) Integrated streamline pattern for the $\langle u \rangle$, $\langle v \rangle$ in-plane velocity components superimposed with out-of-plane vorticity contours. (*bottom*) $\langle u \rangle$, $\langle v \rangle$ velocity vector field shaded by the $\langle w \rangle$ velocity component behind a 3D flapping wing at phase 2 location along the oscillation trajectory. In all cases the velocity components are non-dimensionalised by the freestream velocity U_∞
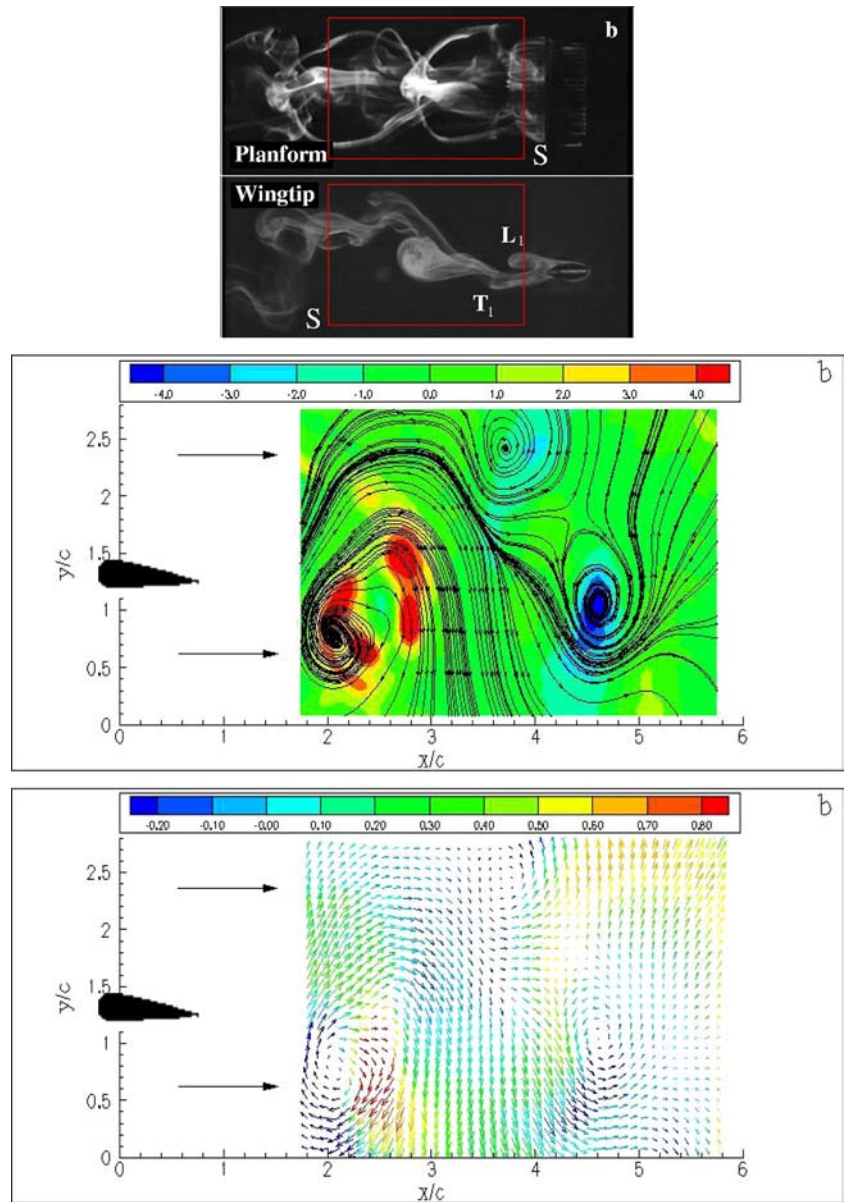
used in the analysis of the PIV images. The time between laser firing d t is calculated so that the maximum size of the measured velocity is $0.25IW_0$ ($=$ maximum velocity ratio, MVR), where IW_0 is the zeroth grid level size corresponding to the initial interrogation area used in the PIV multigrid cross correlation scheme. Similarly, IW_1 is the subsequent grid level of the multi-grid technique. The estimated size of the displacement vector was at most 3.6 px. The MCCDPIV data field is subsequently validated using a mean value check (MVC) of 1.3 standard deviations. The estimated depth of field (dof) was calculated to be 8 px with the current camera setup.

From the PIV images, the three components of velocity u, v and w are calculated and the out of plane vorticity ω_z is derived from the velocity gradients. Instantaneous flow images are acquired at specific phase locations ωt in the heave trajectory of the wing. Based on the variance in the measured velocities, 500 instantaneous image pairs are acquired at each phase in order to resolve the velocities with 1% random error based on a statistical confidence of 99%.

2.4 Stereo PIV analysis

An angular offset stereo configuration is utilized for these measurements. While not as simple as the translation configuration, the limitation of camera angle on a translation system is removed. This is useful for this setup in lieu of physical access limitation in the experimental rig. The details of different stereo configurations are discussed in Prasad and Jensen (1995) and Willert (1997).

Fig. 16 (*top*) Instantaneous dye flow visualization at $St = 0.35$ for phase 3. (*centre*) Integrated streamline pattern for the $\langle u \rangle$, $\langle v \rangle$ in-plane velocity components, superimposed with out-of-plane vorticity contours. (*bottom*) $\langle u \rangle$, $\langle v \rangle$ velocity vector field shaded by the $\langle w \rangle$ velocity component behind a 3D flapping wing at phase 3 location along the oscillation trajectory. In all cases the velocity components are non-dimensionalised by the freestream velocity U_∞
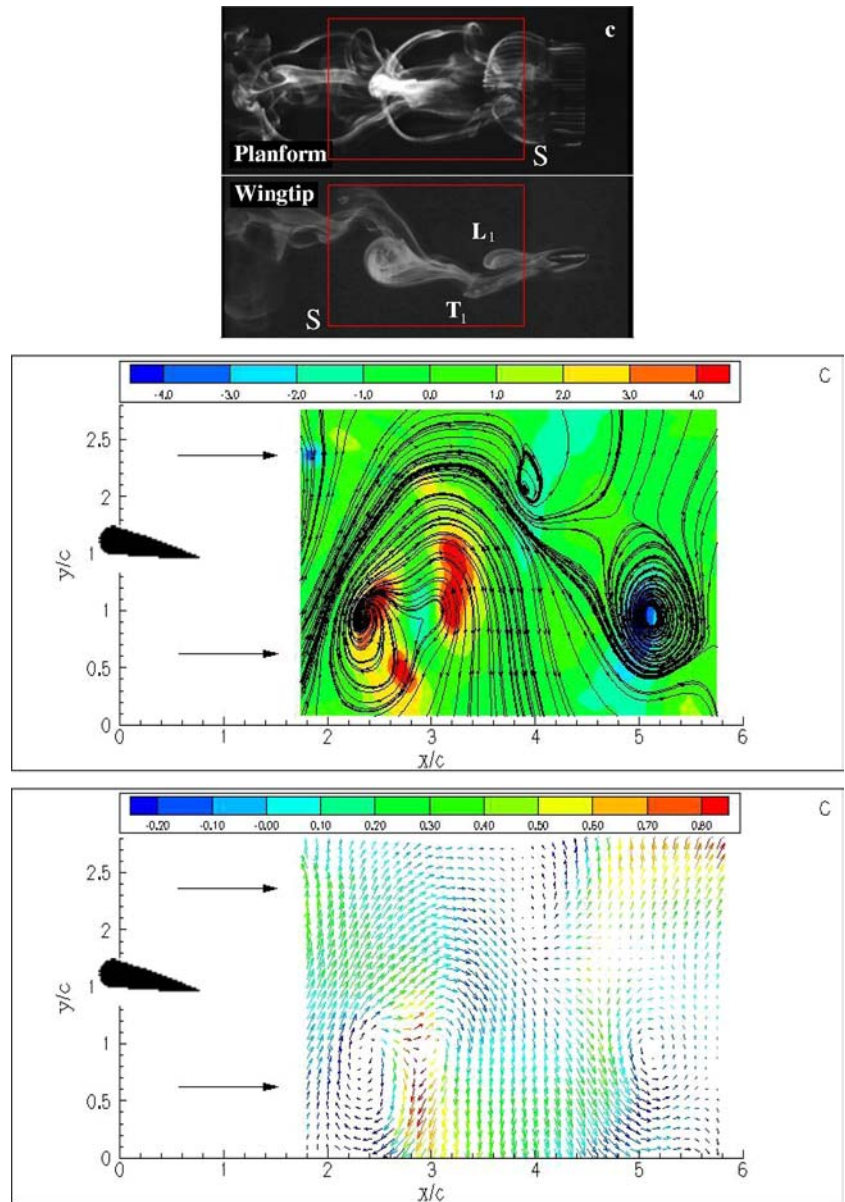
The ability to accurately determine the particle displacements is dependent on how accurately one is able to map from distorted image space to undistorted object space. This is dependent on the calibration process. An in-situ calibration technique, similar to that of Solof et al. (1997), is utilized here as it does not rely on accurate knowledge of the geometry of the stereo-camera setup and is able to account for all distortions encountered during the actual experiment. A 250 mm-square plate with an array of 0.5 mm through-holes (calibration markers) drilled at 5 mm spacings is used as a calibration target. Each camera acquires a calibration image at five equally-spaced planes across a distance corresponding to the thickness of the laser sheet, -1.5 mm $\leq z \leq +1.5$ mm. The accuracy of the calibration is affected also by the number of calibration markers. The third velocity component can only be resolved in calibrated regions common to both cameras. Thus, an adequate number of calibration points are required across the maximum resolvable area. The calibration overlap area is maximized and more than 250 markers are selected to minimise the 3D position error (Chio and Guezennec 1997). During acquisition of the calibration images the calibration plate is illuminated from the back with a halogen lamp mounted in a light box. This arrangement created a black calibration image with an array of white dots as markers. The location of the calibration markers in the distorted image is found using a double locator approach. The ability to accurately locate the calibration markers at peak intensity locations is greatly enhanced by the excellent Gaussian distribution provided by the current back lit calibration setup. Once the peak locator algorithm estimates the location of the calibration markers in the distorted image, a template-matching

Fig. 17 (*top*) Instantaneous dye flow visualization at $St = 0.35$ for phase 4. (*centre*) Integrated streamline pattern for the $\langle u \rangle, \langle v \rangle$ in-plane velocity components superimposed with out-of-plane vorticity contours. (*bottom*) $\langle u \rangle$, $\langle v \rangle$ velocity vector field shaded by the $\langle w \rangle$ velocity component behind a 3D flapping wing at phase 4 location along the oscillation trajectory. In all cases the velocity components are non-dimensionalised by the freestream velocity U_∞
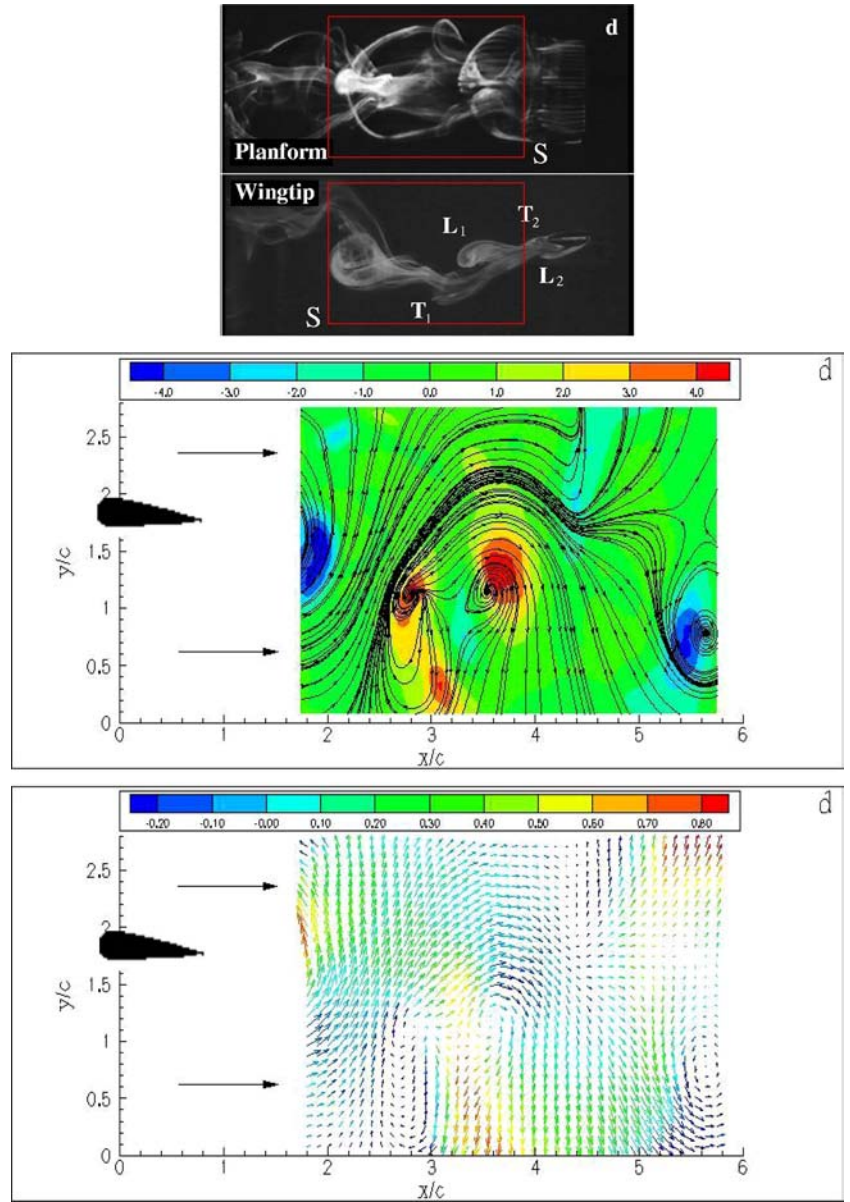
correlation scheme is used to locate the calibration markers to sub-pixel accuracy. The RMS error for locating the marker centres is less than 0.3 px for the x coordinate and 0.2 px for the y coordinate.

The calibration data is used to calculate the mapping function, F, using a least squares approach. Equation 4 shows the vector-valued polynomial F with cubic dependence on the in-plane components x and y, and quadratic dependence on the out-of plane component z. The exponent of the out-of-plane variable in the mapping function F is at best one less than the number of planes measured for calibration. This function is expected to adequately track any distortions one expects to encounter in PIV images (Soloff et al. 1997) and adequately resolve the mapping function with minimal residual error (Willert 1997).

$$
\begin{aligned}
F = {}& a_0 + a_1 x + a_2 y + a_3 z + a_4 x^2 + a_5 xy + a_6 y^2 + a_7 xz \\
& + a_8 yz + a_9 z^2 + a_{10} x^3 + a_{11} x^2 y + a_{12} xy^2 + a_{13} y^3 \\
& + a_{14} x^2 z + a_{15} xyz + a_{16} y^2 z + a_{17} xz^2 + a_{18} yz^2
\end{aligned} \tag{4}
$$

After calibration, the flow is seeded and PIV images are acquired. The in-house developed stereo reconstruction algorithm, StereoMagik, interpolates the displacement information from the two separate PIV images onto a user defined regular grid by applying the mapping function with a bi-linear interpolation scheme. To solve for the fluid displacement, Eq. 6 is solved for Δx, Δy and Δz. Here, ∇F can be calculated from the measured $\underline{x}$ and Eq. 6.

$$
\underline{X} = F \underline{x}, \tag{5}
$$

Fig. 18 (*top*) Instantaneous dye flow visualization at $St = 0.35$ for phase 5. (*centre*) Integrated streamline pattern for the $\langle u \rangle$, $\langle v \rangle$ in-plane velocity components superimposed with out-of-plane vorticity contours. (*bottom*) u, v velocity vector field shaded by the $\langle w \rangle$ velocity component behind a 3D flapping wing at phase 5 location along the oscillation trajectory. In all cases the velocity components are non-dimensionalised by the freestream velocity U_∞
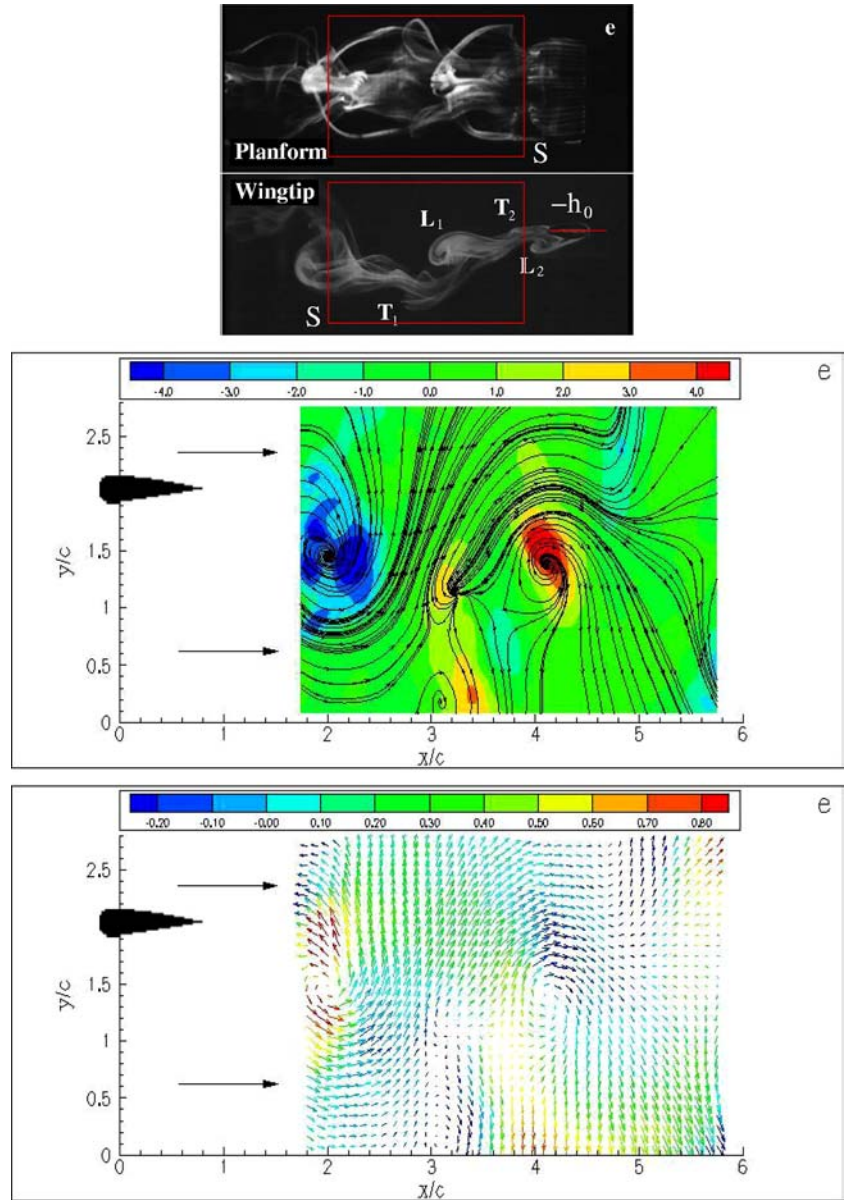
$$\begin{bmatrix} \Delta X^1 \\ \Delta Y^1 \\ \Delta X^2 \\ \Delta Y^2 \end{bmatrix} = \begin{bmatrix} F'_{xx} & F'_{xy} & F'_{xz} \\ F'_{yx} & F'_{yy} & F'_{yz} \\ F'_{zx} & F'_{zy} & F'_{zz} \end{bmatrix} \begin{bmatrix} \Delta x \\ \Delta y \\ \Delta z \end{bmatrix} \qquad (6)$$

Equation 6 represents a simplification of the Taylor expansion of Eq. 5 applied over time Δt. An iterative numerical method is utilized to guarantee root location in order to solve for the fluid displacement in Eq. 6. The StereoMagik algorithm and its application is discussed in greater detail in Parker et al.(2004a, 2004b).

### 2.5 Stereo validation experiments

In SMDPIV the accuracy of the calculated 3D vector field depends primarily on the errors introduced in the 2D PIV measurements, the interpolation of these fields and the calibration process. In order to validate the in-house SMDPIV technique a method similar to Bjork-quist (2001) is adopted in which a known displacement is measured. A synthetic PIV test surface is translated by a fixed distance. The displacement is measured using the SMDPIV technique and $\varepsilon_{\Delta x}$; variation between the actual and measured values is calculated. One hundred and eighty grit sandpaper is used as a test surface.

$$\varepsilon_{\Delta x} = \Delta x_m - \Delta x_t, \qquad (7)$$

where Δx_m is the measured displacement and Δx_t is the true displacement. The accuracy of the fluid to image mapping function can be estimated by using the calibration function to map the calibration marker locations from fluid to image space and then com-

Fig. 19 (*top*) Instantaneous dye flow visualization at $St = 0.35$ for phase 6. (*centre*) Integrated streamline pattern for the $\langle u \rangle$, $\langle v \rangle$ in-plane velocity components superimposed with out-of-plane vorticity contours. (*bottom*) $\langle u \rangle$, $\langle v \rangle$ velocity vector field shaded by the $\langle w \rangle$ velocity component behind a 3D flapping wing at phase 6 location along the oscillation trajectory. In all cases the velocity components are non-dimensionalised by the freestream velocity U_∞
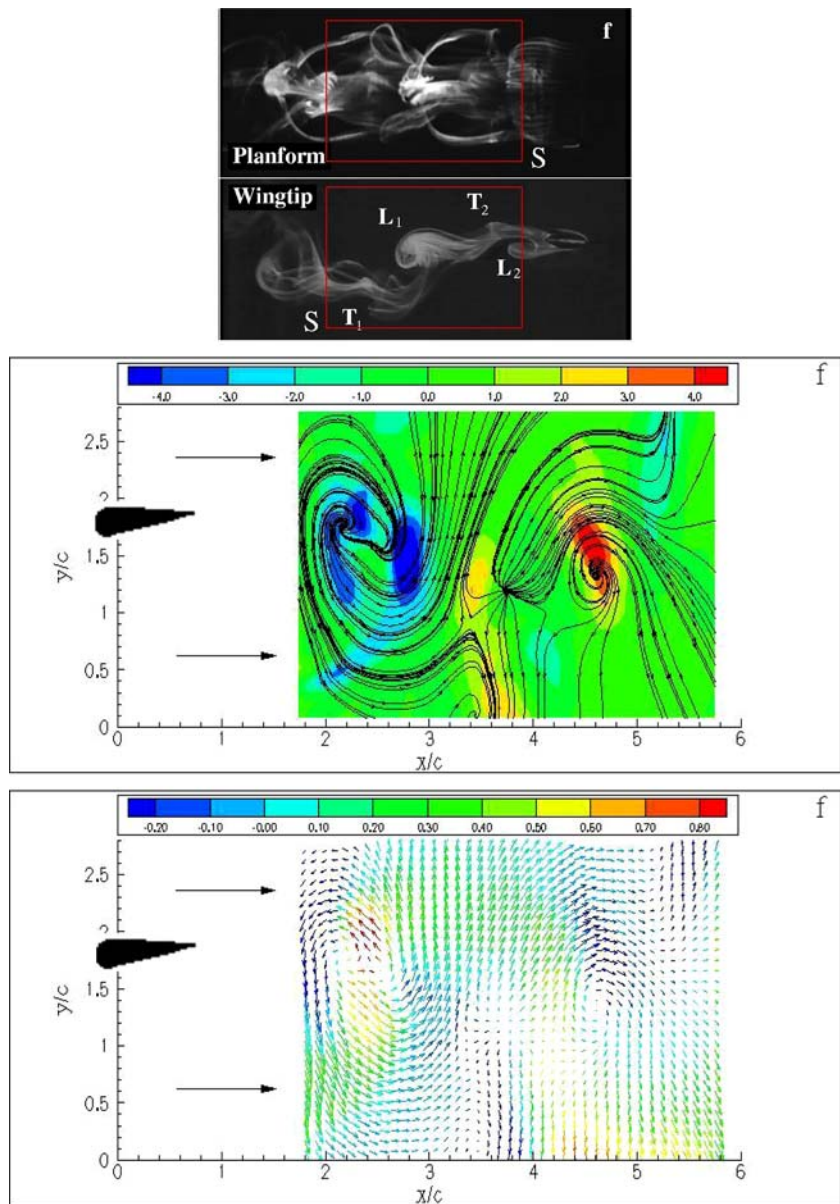
paring them to the marker locations actually recorded for each calibration image. This is referred to as the mapping error. The residuals from the four equations in three unknowns in Eq. 6 indicate the quality of fit of the resolved fluid displacements Δx, Δy and Δz from the measured image displacements ΔX_{left}, ΔY_{left}, ΔX_{right} and ΔY_{right}. This is described as the residual error.

2.6 Stereo validation results and errors

The results from translating the sandpaper 1 mm in all principle directions are shown in Table 3. The uncertainty in the translation of the test surface is 0.001 mm. The values shown represent the RMS of the difference between the measured and actual value. It can be seen that the worst case is when the test block is translated in the z direction. In this case the RMS error in the translated direction is up to eight times as high as the measured y displacement.

Equation 7 is used to calculate the error between the true and measured displacement at each point in the flow field. Figures 7, 8 and 9 represent the errors for displacements in x, y and z, respectively. The data is presented in iso-contours to give an indication of the distribution of error over the measured area. A course grid with $IW_0 = 48$ is used to analyse the data with MCCDPIV. The calibrated region is 60×42 mm in all cases. The greatest error is recorded when the test surface is translated in the z direction. In this case the out-of-plane error is up to ten times greater than the in-plane errors. This is consistent with the work of others (Prasad 2000; Soloff et al. 1997).

Fig. 20 (*top*) Instantaneous dye flow visualization at $St = 0.35$ for phase 7. (*centre*) Integrated streamline pattern for the $\langle u \rangle$, $\langle v \rangle$ in-plane velocity components superimposed with out-of-plane vorticity contours. (*bottom*) $\langle u \rangle$, $\langle v \rangle$ velocity vector field shaded by the $\langle w \rangle$ velocity component behind a 3D flapping wing at phase 7 location along the oscillation trajectory. In all cases the velocity components are non-dimensionalised by the freestream velocity U_∞
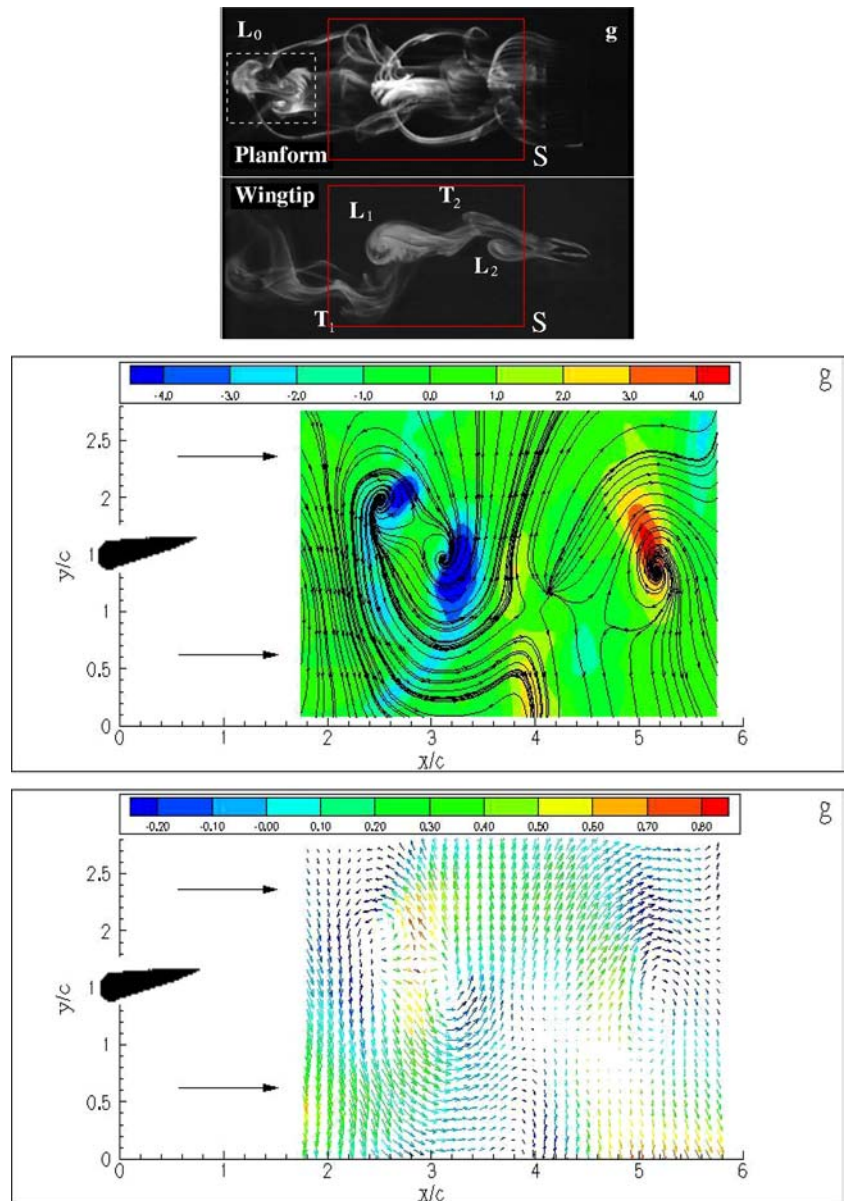

Table 4 indicates the RMS error in locating the calibration markers accurately from the distorted calibration images. These values translate directly into the mapping of particles from distorted to undistorted space. This quantity is dependent on the localization method employed to identify (x, y) coordinates in physical space from the (X, Y) locations in image space. The template correlation scheme utilized here is unique in that a double identification approach is used to identify the calibration marker location in the distorted image. First the distorted calibration image is analysed using a peak intensity location scheme. This is used to create an initial template. Thereafter, the template is cross correlated with the actual distorted image to determine the actual location of the markers to sub-pixel accuracy.

Table 4 indicates the RMS residual error from the final calculation of the fluid displacements. This quantity indicates how accurately the SMDPIV reconstruction algorithm is able to determine the displacements by recalculating the location of the particles in image space once the displacements are determined. The superscripts 1 and 2 indicate the X or Y location of a particle as seen in camera 1 and camera 2, respectively.

The largest residual error originates from the y component of each camera yet the mapping error is greater for the x component. In general, the values are small compared to 48 px, the interrogation window size selected for the PIV analysis of the validation images. If the perspective distortions are actually linear then the use of higher order polynomials, as is the case here, would introduce more error into the solutions for the

Fig. 21 (*top*) Instantaneous dye flow visualization at $St = 0.35$ for phase 8. (*centre*) Integrated streamline pattern for the $\langle u \rangle$, $\langle v \rangle$ in-plane velocity components superimposed with out-of-plane vorticity contours. (*bottom*) $\langle u \rangle$, $\langle v \rangle$ velocity vector field shaded by the $\langle w \rangle$ velocity component behind a 3D flapping wing at phase 8 location along the oscillation trajectory. In all cases the velocity components are non-dimensionalised by the freestream velocity U_∞
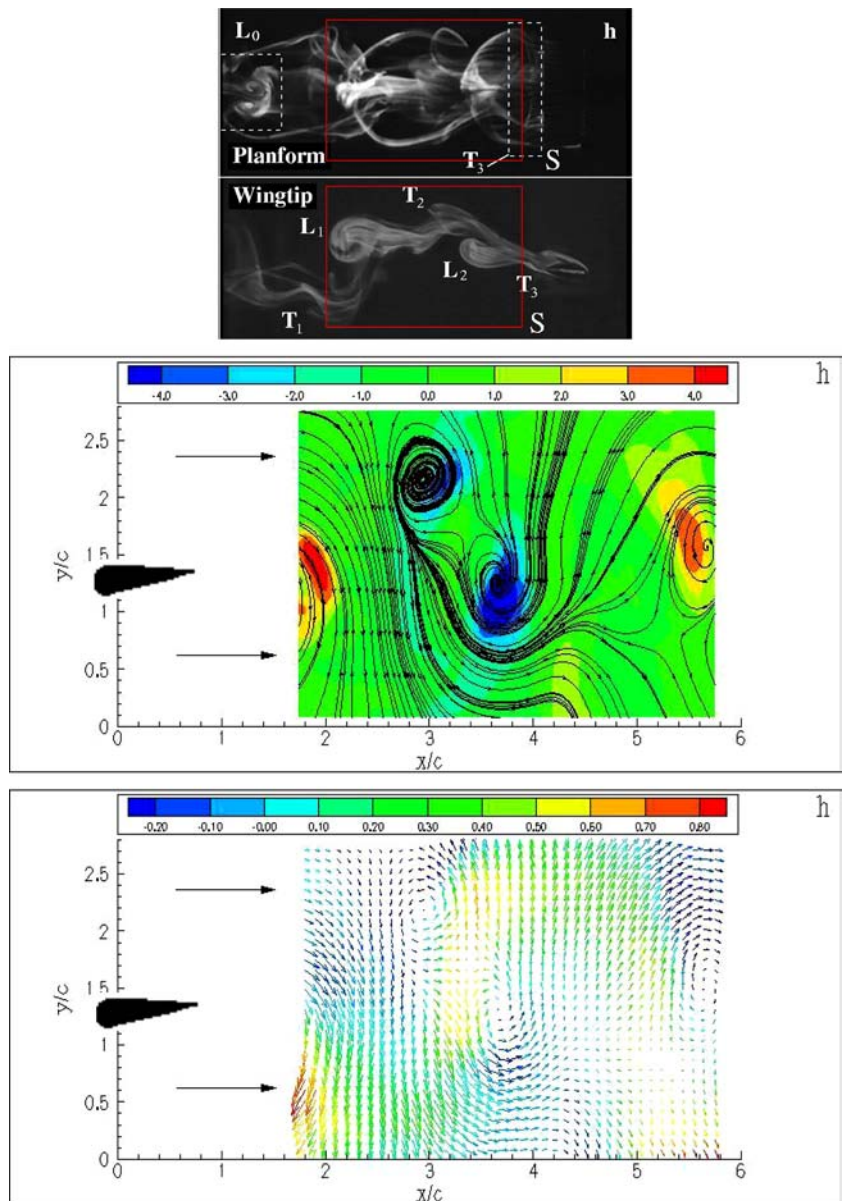
fluid displacements. While the largest RMS error obtained is ten times larger than those obtained by Bjorkquist (2001) it is only 0.0001 mm in the measurement field of 60×42 mm and the measurements are in water as apposed to air.

3 Experimental results

The results of the SMDPIV experiments are presented for $Re = 637$, $\psi = 90°$, $\theta_0 = 5°$ and $St = 0.35$. Instantaneous SMDPIV flow measurements are acquired at eight phase locations in one complete oscillation cycle of the aerofoil. The orientation of the aerofoil at each phase is tabulated in Table 5 and shown in Fig. 10. The measurements are conducted along the mid-plane PP shown in the top image of Fig. 14. Instantaneous images of a

rectangular region S, shown at each phase of the flow visualisation images, are acquired one chord length downstream of the trailing edge of the wing. The $1c$ shift is required due to obstruction caused by the aerofoil in the view of the right camera when viewing from the aerofoil trailing edge. The measurements in Figs. 14–21 are analysed and compared in a reference frame defined in Fig. 11. The aerofoil $c/4$ location is selected as the origin. Since the period of oscillation of the aerofoil is 2 s, any vorticity created at the aerofoil surface will be seen roughly 1 s later within region S. In this time the aerofoil would have moved to another phase location $1s$ later. As a result, any interpretation of the measurements with respect to the aerofoil location must consider this mismatch.

Each of Figs. 14–21 is comprised of three separate images. The top image represents the dye flow visuali-

sation. The centre image is an iso-contour of the vorticity overlaid with the u and v phase-averaged velocity surface streamlines. The lower image is the in-plane vector field shaded by the measured out-of-plane velocity component. These images are grouped together in a figure according to each phase of the aerofoil in order to facilitate comparison. The top right hand letter in each image from Figs. 14–21 corresponds to a specific phase shown in Fig. 10 and mentioned in Table 5 as the figure label. The flow is measured in the plane of symmetry bisecting the aerofoil span where dye flow visualizations show that the flow exhibits greatest complexity. In all the fields presented in this paper the flow is from left to right while in the corresponding flow visualisations the flow direction is reversed. A cartoon of the aerofoil inserted in each image is to scale and has been placed in the correct location relative to the SMDPIV measured region. The orientation of the aerofoil provides a relative sense of the resulting flow morphology.

3.1 Flow visualisations

The flow visualization data presented in the top image of Figs. 14–21 represent a volume of illuminated flow integrated over the entire wing span. In the wingtip and planform views shown, the camera captures and records regions in the flow from where the most light is scattered, and these correspond to regions of concentrated dye. A comprehensive analysis and discussion of this data is presented in (von Ellenrieder et al. 2003). From the wingtip view the image includes all visible effects across the span of the wing. The dye images are inverted compared to the PIV images due to the use of a mirror during filming (von Ellenrieder et al. 2003). Each image provides an integrated view of the flow. Vortices are identified as L and T indicating a leading and trailing edge vortex, respectively. The subscripts 1 and 2 indicate to which pair of shed vortices a particular vortex belongs. This abbreviation will be used to denote the comparative structures in the discussion. The location of $+h_0$ and $-h_0$ have been clearly marked in Figs. 14 and 18, respectively.

3.2 Phase averaged 2D 3C measurements

The average velocities $\langle u \rangle$, $\langle v \rangle$ and $\langle w \rangle$ are calculated at each phase and the in-plane integrated streamline patterns are shown in the centre image of Figs. 14–21. From the phase averaged velocities the in-plane spatial gradients are used to calculate the phase averaged out-of-plane vorticity $<\omega_z>$ using a local least squared approach. The vorticity is non-dimensionalised by the forced oscillatory time scale, $\dot{h}_{max}/A$. Initially, the maximum angular velocity $\dot{\theta}_{max}$ of the pitch oscillation was used but the vortex shedding appeared to have a greater dependence on the maximum heave

oscillation velocity $\dot{h}_{max}$ than $\dot{\theta}_{max}$ which is six times smaller than $\dot{h}_{max}$. Furthermore, this timescale is selected over a convective timescale U_∞/c since $\dot{h}_{max}/A$ dominates the mean flow and appears to be responsible for the large disturbances in the flow. The accuracy of the calculated vorticity is dependant on the spatial separation of each velocity measurement Δ and the characteristic length scale of the structures being measured. Full details of the calculation method as well as the accuracy is discussed in Fouras and Soria (1998). For the vorticity distribution with a length scale of 16Δ, the bias error is estimated as 0.4% and the random error is estimated as $\pm2.1\%$ at the 99% confidence level. The bias error in the derived vorticity distribution is 3.4% and the random error is estimated as $\pm0.9\%$ at the 99% confidence level. Negative vorticity is out of the page.

The vorticity iso-contours are superimposed onto the $\langle u \rangle \langle v \rangle$ streamlines. The streamlines are confined to the 2D projection of the flow in xy space and are calculated from the $\langle u \rangle$ and $\langle v \rangle$ phase-averaged components of velocity integrated along the freestream direction. Streamlines are not Galilean invariant because they depend on the velocity of the observer. The complexity arises when integrated particle paths cross instantaneous streamlines creating ambiguous structures (Chong et al. 1990). Nonetheless, their purpose here is to show the nature of the in-plane vector field flow in relation to closed orbits or spirals. The convection velocity U_∞ is removed in order to obtain the frame of reference of an observer moving with the fluid.

The z component of velocity is used to shade the x and y-component velocity vector field. This data is presented as the bottom image of Figs. 14–21. The convection velocity is subtracted from the non-dimensionalised velocity $\langle u \rangle/U_\infty$. Every second vector is shown.

3.3 Mean flow measurements

The properties of the time-mean flow field are calculated by adding all the phase averaged velocities as shown in Eq. 8. The non-dimensionalised in-plane vector field, u/U_∞ and v/U_∞, is shown in Fig. 12 with mean profiles highlighted at $x/c = \{2.0, 2.8, 3.6, 4.8, 5.8\}$. These locations were randomly selected to look at the variation in the freestream direction. Every second vector is shown.

$$\mathbf{u}(x,y,z) = \frac{1}{8}\sum_{\phi=1}^{8} \langle\mathbf{u}(x,y,z)\rangle_\phi \tag{8}$$

4 Discussion of results

The mean velocity profiles in Fig. 12 have a jet-like profile with symmetry about the mean heave axis at

$y/c = 1.5$. The velocity addition in the wake region is indicative of net thrust production. The word 'wake' here is meant to refer to the region behind the trailing edge. This is most evident at $x/c < 4$, where the wake width is small enough to be captured in its entirety. Further downstream the wake grows and the jet-like profile is not as obvious. At $x = 2c$ the wake width is roughly $2c$. The width here is measured from the first occurrence of the freestream velocity on either end of the profile. The double hump measured at $x/c = 2.8$ is due to the vortex pairs discussed later that shed on either side of the mean heave axis at $h = 0$.

From the wingtip view of the dye-flow visualizations, two pairs of vortices are shed in one complete cycle in the sequence. In the region S this appears in the order

$$T_1 \rightarrow L_1 \rightarrow T_2 \rightarrow L_2. \tag{9}$$

The evolution of spanwise ω_z vorticity over one cycle is characterised by regions of intense counter-rotating vorticity that group together about the mean heave axis to form a reverse Karman vortex street. The maximum heave velocity is $\dot{h}_0 = O(U_\infty)$. If it is assumed that all vortices formed at the aerofoil convect at the same convection velocity in the x and y directions, simple equations of motion can be used to determine the proximity of shed vorticity to the origin shown in Fig. 11 at different temporal stations. Figure 13 is a sketch of the morphology of structures that are created due to the motion of the flow relative to the aerofoil. This interpretation of the flow is independent of the measurements and based purely on the kinematics of the aerofoil and expectation of the flow behaviour from fluid mechanics. The sketch provides qualitative information of the spatial scale and direction of vorticity with some consideration of convection of the vortices due to self induction and the mean flow. The birth of vorticity at the leading and trailing edges have been appropriately labelled while the sequence of alphabets on the left correspond to the phase locations described in Table 5.

Figure 13 shows that the flow is expected to be populated by pairs of co-rotating vortices that shed in the sequence described by Eq. 9 and observed in the flow visualisations. From the relative x and y tangential velocities the direction of roll-up of vorticity at the leading edge can be inferred. This is shown in Fig. 13a, e. When the aerofoil is oriented at the extreme pitch angles, $-\theta_0$ and $+\theta_0$ in Fig. 13c and g respectively, the Kutta condition imposes a flow separation condition at the trailing edge, resulting in the formation of T-vortices. The sequence of events and the resulting flow pattern depicted in Fig. 13 are similar to the results of Anderson (1996) from 2D PIV measurements as well as comments by others at similar experimental conditions (Guglielmini and Blondeaux 2004; Triantafyllou et al. 2004). Furthermore, Gugliemini and Blondeaux (2004) comment that the L vortex is a strong dynamic stall vortex that amalgamates with a weaker T vortex of similar sign in the case of $2A/c \geq 1$, thus setting up a Karman vortex street in the mean flow with the second vortex pair of opposite sign.

From the vorticity measurements the flow field is characterised by symmetrical shedding of regions of opposite vorticity into a reverse Karman vortex street. At phase 1 in Fig. 14 two adjacent regions of counter-clockwise (CCW) rotating vortices appear to enter the measurement region S on the left hand side of the centre image. The spanwise vorticity appears to be connected at this stage. At this phase the flow visualisation image shows T_1 and L_1 entering region S while preceded by the unmarked L and T vortices from the previous cycle. At this phase the aerofoil is at $+h_0$, $\theta = 0°$ and the resultant of the relative tangential heave and freestream velocity is expected to promote flow rotation in the clockwise (CW) direction resulting in $-\langle w_z \rangle$. This can be seen in Fig. 13a. However, the $-\langle w_z \rangle$ appearing at phase 1 is from vorticity 1 s old, when the aerofoil was at $-h_0$, phase 5, as in Fig. 18. The location of foci in the streamline patterns of Fig. 14 correspond to regions of intense vorticity. This suggests that in this case the structures are convecting at the same convection speed subtracted from the mean fields. While velocity fields are not Galilean invariant, the in-plane vector field shows regions of circulating flow corresponding to the foci and intense spanwise vorticity. Furthermore, regions of intense $-\langle w_z \rangle$ correspond to regions of relatively large $-\langle w \rangle$ velocity components. These have a magnitude of roughly $0.2U_\infty$.

At phase 2, the flow has evolved over 0.25 s and the structures would have convected $1/3c$ as shown in Fig. 13b. The vorticity contour in Fig. 15 shows that the $+\langle w_z \rangle$ region previously observed is more distinguishable as two regions. In general the concentrated regions of vorticity have convected further downstream as well as spread in the y direction. The flow visualisation image shows L_1 and T_1 separated a distance of roughly $0.5c$. In this case the streamline pattern does not have a focus corresponding to all regions of vorticity, suggesting a change in the convective properties of the structures from the previous phase. The distribution of f$\langle w \rangle$ velocity in the in-plane vector field is suggestive of highly three-dimensional flow. In this case any structures would move through the measurement plane.

At phase 3 in Fig. 16 the aerofoil has reached the maximum angle of attack. Imposition of the Kutta condition at the sharp trailing edge would result in the formation of a CCW T-vortex similar to Fig. 13c. The effect of this event will be observable in region S, 1 s later in phase 5, Fig. 18. The spacing between regions of strong vorticity has increased by a greater margin than in previous phases. This observation is also made for phase 7 when the aerofoil is at the minimum angle of attack. Perhaps this effect is due to the formation of the T vortex, which is a relatively violent event in the motion of the aerofoil.

At phase 4, Fig. 17, T_2 first appears in the flow visualisation. This coincides with the first appearance of $-\langle w_z \rangle$ in the vorticity field. The spacing between vorticity

regions remain relatively unchanged from the previous phase. The in-plane vector field maintains an undulating profile with a staggered array of concentrated vorticity. The region of $+\langle w_z \rangle$ on the right of the vorticity contour plot is weaker than the adjacent $+\langle w_z \rangle$ region. Given the inherent complexity of this 3D flow more spatial information is required to determine causality. Nonetheless, continual weakening of the observed $+\langle w_z \rangle$ region is noticed in subsequent phases. Besides appearing to weaken, the roll-up of the streamline patterns at subsequent phases suggests that the structure has slowed down and is no longer convecting at the same speed as the other regions. On approach of $-h_0$ in phase 5 the evolutionary properties of the vorticity and velocity fields are reversed. Through self induction and mean-flow convection the two regions of $+\omega_z$ have moved in opposite directions and have moved apart by a distance greater than $1c$. At phases 5 and 7 where L_2 and T_2 are created as in Fig. 13e and g, respectively, vortical structures enter region S in the corresponding dye-flow images. While there is a 1 s delay due to the relative point of inception and point of measurement, introduction of two regions of vorticity is seen at subsequent phase images. The rotation of these regions of vorticity correspond to the expected circulation from Fig. 13. From the single plane of measurement it is difficult, or near impossible, to determine accurately the morphology of the complex 3D flow structures in this unsteady flow. There are techniques that can unambiguously resolve any complex flow field and identify the topology (Soria et al. 1996). These require more 3D velocity information along the span of the aerofoil.

5 Conclusions

1. The SMDPIV approach adopted for this study is able to provide accurate and repeatable measurements of an unsteady oscillatory flow applied to a liquid flow environment. Some of the refinements introduced in this paper have optimised the experimental methodology and reduced the measurement error.
2. From the jet-like mean velocity profile it can be inferred that the 3D flapping wing is able to produce net thrust. The flow is characterised by a reverse Karman vortex street associated with thrust production.
3. The measurements correspond to both experimental and numerical studies conducted elsewhere and support the theory that in the initial stages of development spanwise vorticity of similar sign amalgamate on either side of the mean heave axis for the counter rotating street. Structures inferred from the dye-flow visualisations are identifiable and can be related to the SMDPIV measurements.
4. While the w velocity is relatively small compared to U_∞, regions of intense spanwise vorticity coincide with regions of relatively large out-of-plane velocity. None-

theless, more 2D 3C information is required in multiple planes along the aerofoil span in order to adequately extract the spatial detail of the flow geometry.

References

Anderson JM (1996) Vortex control for efficient propulsion. PhD Thesis, Massachusetts Institute of Technology and Woods Hole Oceanographic Institute, February 1996

Anderson JM, Streitlien K, Barrett DS, Triantafyllou MS (1998) Oscillating foils of high propulsive efficiency. J Fluid Mech 360:41–72

Bjorkquist D (2001) Design and calibration of a stereoscopic PIV system. In: Proceedings of 9th international symposium on applied laser techniques to fluid mechanics, Lisbon, Portugal, pp 13–16

Blondeaux P, Fornarelli F, Guglielmini L, Triantafyllou MS, Verzicco R (2005) Vortex structures generated by a finite-span oscillating foil. 43rd AIAA aerospace sciences meeting and exhibit, 10 January 2005, paper 1030-84

Cheng HK, Murillo LE (1984) Lunate-tail swimming propulsion of curved lifting line in unsteady flow. Part 1. Asymptotic theory. J Fluid Mech 143:327–350

Chio W, Guezennec YG (1997) In-situ calibration for wide-angle, three-dimensional stereoscopic image analysis. Appl Opt 36(29):7364–7372

Chong MS, Perry AE, Cantwell BJ (1990) A general classification of three-dimensional flow fields. Phys Fluids 2(5):765–777

DeLaurier JD, Harris JM (1982) Experimental study of oscillating wing propulsion. J Aircraft 19(5):368–374

Dong H, Mittal R, Bozkurrtas M, Najjar F (2005) Wake structure and performance of finite aspect-ratio flapping foils. 43rd AIAA aerospace sciences meeting and exhibit, 10 January 2005, paper 900-81

Drucker EG, Lauder GV (2001) Wake dynamics and fluid forces of turning maneuvers in sunfish. J Exp Biol 204:431–442

Fouras A, Soria J (1998) Accuracy of out-of-plane vorticity measurements using in-plane velocity vector field data. Exp Fluids 25:409–430

Gopalkrishnan R, Triantafyllou MS, Triantafyllou GS, Barrett D (1994) Active vorticity control in a shear layer using a flapping foil. J Fluid Mech 274:1–21

Guglielmini L, Blondeaux P (2004) Propulsive efficiency of oscillating foils. Euro J Mech B-Fluids 23:255–278

Jones KD, Castro BM, Mahmoud O, Pollard SJ, Platzer MF, Neef MF, Gonet K, Hummel D (2002) A collaborative numerical and experimental investigation of flapping-wing propulsion in ground effect. AIAA paper 2002-706, Reno, Nevada, January 2002

Jones KD, Dohring CM, Platzer MF (1998) Experimental and computational investigation of the Knoller-Betz effect. AIAA J 36(7):1240–1246

Karpouzian G, Spedding G, Chen HK (1990) Lunate-tail swimming propulsion. J Fluid Mech 210:329–351

Katz J, Weihz D (1978) Behaviour of vortex wakes from oscillating airfoils. J Aircraft 50(12):861–863

Koochesfahani MM (1989) Vortical patterns in the wake of an oscillating airfoil. AIAA J 27(9):1200–1205

Lawson NJ, Wu J (1997) Three-dimensional particle image velocimetry: error analysis of stereoscopic techniques. Meas Sci Technol 8:1455–1464

McCroskey WJ (1982) Unsteady airfoils. J Fluid Mech 14:285–311

Ohmi K, Coutanceau M, Daube O, Loc TP (1991) Further experiments on vortex formation around translating airfoils at large incidences. J Fluid Mech 225:607–630

Ohmi K, Coutanceau M, Duliec A, Loc TP (1990) Vortex formation around an oscillating and translating airfoil at large incidences. J Fluid Mech 211:37–60

Parker K, von Ellenrieder K, Soria J (2002) The effects of phase angle on the vortical signatures behind a flapping airfoil of finite aspect ratio. In: Proceedings of 10th international symposium flow visualization, Kyoto, Japan, 26-29 August 2002

Parker K, von Ellenrieder K, Soria J (2003a) Flow visualization of the effect of pitch amplitude changes on the vortical signatures behind a three dimensional flapping airfoil. Proceedings SPIE 5058:331-343

Parker K, von Ellenrieder K, Soria J (2003b) Strouhal number dependance of the vortex aspect ratio behind a three dimensional heaving airfoil. In: Proceedings of 2nd international conference on heat transfer, fluid mechanics and thermodynamics, Zambia. HEFAT, June 23–26

Parker K, von Ellenriedern K, Soria J (2004a) A description of the vortical skeleton behind an finite-span flapping wing. In: Proceedings of 12th international symposium on applications of laser techniques to fluid mechanics, Lisbon, Portugal

Parker K, von Ellenrieder K, Soria J (2004b) Stereoscopic PIV measurements of the flow past a circular cylinder at Reynolds number 15,000. In: Proceedings of 15th Australasian fluid mechanics conference, University of Sydney, New South Wales, Australia, AFMC

Platzer MF (2001) Flapping wing propulsion. Technical report, Naval Postgraduate School, Monterey

Prasad AK (2000) Stereoscopic particle image velocimetry. Exp Fluids 29:103–116

Prasad AK, Jensen K (1995) Scheimpflug stereocamera for particle image velocimetry in liquid flows. Appl Opt 34(30):7092–7099

Ramamurti R, Sandberg WC (2001) Computational study of 3-d flapping foil flows. AIAA Paper 2001-0605, Washington, DC

Soloff SM, Adrian RJ, Liu ZC (1997) Distortion compensation for generalized stereoscopic particle image velocimetry. Meas Sci Technol 8:1441–1454

Soria J (1996) An adaptive cross-correlation digital PIV technique for unsteady flow investigations. In: Masri AR, Honnery DR (eds) Proceedings of 1st Australian conference on laser diagnostics in fluid mechanics and combustion, University of Sydney, Sydney, December 1996, pp 29–48

Soria J, New TH, Lim TT, Parker K (2003) Multigrid CCDPIV measurements of accelerated flow past an airfoil at an angle of attack of 30 degrees. Exp Thermal Fluid Sci 27:667–676

Soria J, Ooi A, Chong MS (1996) Volume integrals of the $q_A - r_A$ invariants of the velocity gradient tensor in incompressible flow. Fluid Dyn Res 19:219–233

Triantafyllou GS, Triantafyllou MS, Grosenbaugh MA (1993) Optimal thrust development in oscillating foils with application to fish propulsion. J Fluid Struct 7:205–224

Triantafyllou MS, Techert AH, Hover FS (2004) Review of experimental work in biomimetics foils. J Oceanic Eng 29:585–594

von Ellenrieder K, Parker K, Soria J (2001) Visualization of the three-dimensional flow behind heaving foils. In: Proceedings of the 14th Australasian fluid mechanics conference, University of Adelaide, AFMC, 11–14 December 2001

von Ellenrieder KD, Parker K, Soria J (2003) Flow structures behind a heaving and pitching finite-span wing. J Fluid Mech 490:129–138

Willert C (1997) Stereoscopic digital particle image velocimetry for application in wind tunnel flows. Meas Sci Technol 8:1465–1479